The 9th European Congress on Computational Methods in Applied Sciences and Engineering
ECCOMAS Congress 2024
3–7 June 2024, Lisboa, Portugal

# COMPETITION BETWEEN 2D AND 3D AERODYNAMIC STALL MODES IN TRANSITIONAL FLOWS AROUND A NACA0012 AIRFOIL AT $Re$ =90000.

**Konstantinos Sarras**[1] **and Olivier Marquet**[1]

[1] ONERA-DAAA
Institut Polytechnique de Paris
8 rue des Vertugadins, 92190 Meudon, France
e-mail: konstantinos.sarras@onera.fr

**Key words:** Linear stability, Transitional Flows, Airfoil stall

**Summary.** Turbulent and transitional flows around airfoils near stalling conditions may be characterized by low-frequency oscillations during which the flow alternates between attached and detached states, or by stall cells, that induce a spanwise modulation of the flow on the suction side of the airfoil. In this paper we investigate the onset of such phenomena for the transitional flow over a NACA 0012 airfoil at the Reynolds number $Re = 90000$ using global stability analysis. The transitional nature of the flow is modelled using the linear eddy-viscosity model developed by Spalart & Allmaras that is coupled here with a correlation-based algebraic transition model. Steady-state solutions of the aforementioned system reveal a characteristic inverted-S shape curve with two saddle-node bifurcations. The global stability analysis of these steady solutions is based on the full linearization of the governing discrete equations, including the turbulence model, the transition model and the numerical stabilization terms. It reveals the existence of two unstable modes: a two-dimensional low-frequency (unsteady) mode and a three-dimensional zero-frequency (steady) mode. The competition between these two modes is investigated by following their corresponding eigenvalues along the branches of steady solutions. We have identified the critical angles for each mode and shown that the three-dimensional modes become unstable prior to the two-dimensional ones, for this particular case.

## 1 INTRODUCTION

Airfoil stall is commonly described as a sudden drop of lift when increasing the angle of attack past a critical value. This drop of lift is related to a sudden change of the flow topology, where the flow alters from an attached to a massively separated state and can lead to detrimental effects in aeronautical applications. Airfoil stall is associated with many complex physical phenomena that are commonly observed in experiments such as flow hysteresis, low-frequency oscillations and/or stall cells. Flow hysteresis was firstly observed in the experiments of [1] and is related to co-existing solutions of the fluid system for the same angle of attack; In this sense, for the same angle of attack $\alpha$ one can observe either an attached or a fully detached (stalled) flow state depending on whether the configuration is reached by increasing or decreasing the angle $\alpha$. The low-frequency oscillations phenomenon of stalled airfoils was investigated by [2], who where the first to confirm that it was due to a natural flow oscillation rather than a structural vibration. This phenomenon is observed as a high-amplitude oscillation of the unsteady force coefficients

and manifests a periodic alternation of the flow topology between the attached and the separated state. The non-dimensional Strouhal number based on the chord $c$ and the freestream velocity $U_0$ is typically very low ($St \sim 0.02$), an order of magnitude smaller than the shedding frequency $St \sim 0.2$. Recently, [3] showed that this phenomenon is linked to the destabilization of a two-dimensional global mode, for an airfoil in a fully turbulent flow regime at $Re \sim 10^6$ exhibiting trailing edge stall. Lastly, stall cells are three-dimensional cellular patters that appear on the suction side of the airfoil near the stalling angle of attack. Identified experimentally since the seventies by [4] and [5], they result in a time-independent periodic modulation of the separation line in the spanwise direction. This phenomenon has been shown by [6] to be related to the destabilization of a three-dimensional stationary global mode on a fully turbulent airfoil at $Re = 350000$. The aim of this paper is twofold; Firstly, we study the onset of steady and unsteady phenomena on an airfoil experiencing static hysteresis in transitional flow conditions, extending thus the works of [3] and [6] that where in fully turbulent conditions. Secondly, we examine how the two types of instabilities compete with each other along the branches of co-existing steady solutions, identifying which instability is the primary one.

## 2 METHODOLOGY

### 2.1 Governing equations for the transitional flow

In this paper we investigate the transitional flow around a NACA 0012 airfoil at a Reynolds number $Re = U_0 c/\nu = 90000$, where $U_0$ is the free-stream velocity, $c$ is the chord of the airfoil and $\nu$ is the kinematic viscosity. In the following, $c$ and $c/U_0$ are the characteristic length and time scales that are used to non-dimensionalize all variables. We solve for the incompressible transitional flow which we model in the framework of the Reynolds-Averaged Navier-Stokes (RANS). The flow governing equations, in a non-dimensional form, read

$$\frac{\partial \mathbf{u}}{\partial t} + (\mathbf{u}\cdot\boldsymbol{\nabla})\mathbf{u} = -\boldsymbol{\nabla} p + \boldsymbol{\nabla}\cdot\left[\left(\frac{1}{Re} + \nu_t(\tilde{\nu})\right)\mathbf{S}(\mathbf{u})\right] \quad , \quad \boldsymbol{\nabla}\cdot\mathbf{u} = 0, \tag{1}$$

where $\boldsymbol{\nabla} = (\partial_x, \partial_y, \partial_z)^T$, $\mathbf{u} = (u, v, w)^T$ is the mean velocity field, $p$ the mean pressure field and $\mathbf{S}(\mathbf{u}) = \boldsymbol{\nabla}\mathbf{u} + (\boldsymbol{\nabla}\mathbf{u})^T$ the strain-rate tensor. Here, the Reynolds stresses are modelled through the effect of the eddy-viscosity field $\nu_t$ ( linear eddy-viscosity model) which appears as additive viscosity term. The eddy-viscosity $\nu_t$ is a function of the turbulent variable $\tilde{\nu}$ which is governed by the Spalart-Allmaras transport equation

$$\frac{\partial \tilde{\nu}}{\partial t} + (\mathbf{u}\cdot\boldsymbol{\nabla})\tilde{\nu} = \gamma\cdot c_{b1}\tilde{S}\tilde{\nu} - c_{w1} f_w \left(\frac{\nu}{d}\right)^2 + \frac{1}{\sigma}\boldsymbol{\nabla}\cdot\left[\left(\frac{1}{Re} + \tilde{\nu}\right)\boldsymbol{\nabla}\tilde{\nu}\right] + c_{b2}\boldsymbol{\nabla}\tilde{\nu}\cdot\boldsymbol{\nabla}\tilde{\nu},$$
$$\nu_t(\tilde{\nu}) = f_{v1}(\tilde{\nu}). \tag{2}$$

For the detailed definition of the functions and constants of the model we refer to [7]. On the right-hand-side, the intermittency function $\gamma$ that premultiplies the production term models the transitional nature of the flow; in the laminar regions, $\gamma = 0$ and therefore there is no production of turbulence. As a result, the levels of $\nu_t$ are negligible compared to the kinematic viscosity $\nu$ and the RANS momentum operator reduces to the classical Navier-Stokes equations. In the turbulent region, the function saturates to $\gamma = 1$, initiating production of turbulence and increasing the levels of $\nu_t$. We determine the intermittency function here using the algebraic

transition model of [8], which calculates $\gamma$ as

$$\gamma = 1 - e^{(\sqrt{T_1} - \sqrt{T_2})} \tag{3}$$

where the terms $T_1$ and $T_2$ are given by

$$T_1 = \frac{max(Re_\theta - Re_\theta^c, 0)}{\chi_1 Re_\theta^c}, \quad T_2 = max\left(\frac{\nu_t}{\chi_2}\right) \tag{4}$$

where $\chi_1 = 0.002$ and $\chi_2 = 0.02$ are constants of the model and the $Re_\theta$ number is based on the vorticity Reynolds number $Re_\Omega$ which is given by

$$Re_\theta = Re_\Omega / 2.193, \quad Re_\Omega = \Omega d^2 Re \tag{5}$$

with $\Omega$ being the vorticity and $d$ the normal distance to the walls. The first $max$ function in equation 4 activates $\gamma$ when $Re_\theta$ exceeds a critical value $Re_\theta^c$ which is empirically given by correlations as

$$Re_\theta^c = 803.73(Tu_\infty - 0.6067)^{-1.027} \tag{6}$$

where $Tu_\infty$ is the intensity of freestream turbulence which is considered in this study as $Tu_\infty = 0.01$. To impose laminar inflow condition, [8] suggest the far-field boundary condition for $\tilde{\nu}$ in the Spalart transport equation to be $\tilde{\nu} = (0.015 - 0.025)\nu$.

### 2.2 Newton's method and continuation method for identifying co-existing solutions

The governing RANS (1), Spalart-Allmaras (2) and transition model (3) equations may be re-written in the following operator form

$$\mathcal{M}\frac{\partial \boldsymbol{q}}{\partial t} = \mathcal{R}(\boldsymbol{q}, \alpha) \tag{7}$$

where $\boldsymbol{q} = (u, v, w, p, \nu_t, \gamma)^T$ is the state vector that gathers all variables of the problem and $\mathcal{R}(\boldsymbol{q}, \alpha)$ is the residual vector of the governing equations. We note that the system of equations (7) is a function of the angle of incidence $\alpha$ that is a free parameter in our problem. For a specific angle of incidence $\alpha_0$ we seek for the two-dimensional steady state solution $\boldsymbol{q_0} = (u_0, v_0, 0, p_0, \nu_{t0}, \gamma_0)^T$ of the governing equations, i.e. the $\boldsymbol{q_0}$ that satisfies $\mathcal{R}(\boldsymbol{q_0}, \alpha_0) = \boldsymbol{0}$. When fixing the angle $\alpha_0$, we can formally obtain such fixed point solutions in an iterative manner using the Newton's method which produces successively better approximations $\boldsymbol{q_0}^{n+1}$ over the previous solution $\boldsymbol{q_0}^n$ by updating the state vector as

$$\boldsymbol{q_0}^{n+1} = \boldsymbol{q_0}^n - \eta^{n+1}\mathcal{L}^{-1}\mathcal{R}(\boldsymbol{q_0}^{n+1}, \alpha_0) \tag{8}$$

where $\eta^{n+1} \in (0.1]$ is a relaxation factor that aids convergence and $\mathcal{L} = \frac{\partial \mathcal{R}}{\partial \boldsymbol{q}}(\boldsymbol{q_0}, \alpha_0)$ is the Jacobian operator, i.e. the linearization of the governing equations around the steady-state $\boldsymbol{q_0}$ at the angle $\alpha_0$. The Jacobian operator $\mathcal{L}$ is obtained by the linearization of the full-set of governing equations; it is therefore composed of a laminar diagonal block which corresponds to the linearization of the Navier-Stokes operator, a turbulent/transition diagonal block corresponding

to the linearization of the turbulence and transition models and of the off-diagonal blocks that couple the laminar and turbulent variables. Near stall though, equation 8 exhibits co-existing solutions for the same angle of attack $\alpha_0$ due to flow hysteresis. This is manifested in the polar curve $C_L-\alpha$ (where $C_L$ is the lift coefficient) as the $C_L(\alpha)$ function being non-injective (not 1:1). The inverse function though $\alpha(C_L)$ is indeed injective at high $\alpha$ as there is a unique solution of $\alpha$ for each $C_L$. In view of this, instead of fixing $\alpha_0$ we can instead fix a target value for the lift coefficient $C_L^t$ and solve the non-linear equations

$$\begin{pmatrix} \mathcal{R}(\boldsymbol{q_0}, \alpha_0) \\ C_L(\boldsymbol{q_0}, \alpha_0) - C_L^t \end{pmatrix} = \begin{pmatrix} \boldsymbol{0} \\ 0 \end{pmatrix} \tag{9}$$

where $C_L(\boldsymbol{q_0}, \alpha_0)$ is the lift coefficient and the angle of attack $\alpha_0$ is an unknown. A Newton method is used to solve this augmented nonlinear system, leading to

$$\begin{pmatrix} \boldsymbol{q_0} \\ \alpha_0 \end{pmatrix}^{n+1} = \begin{pmatrix} \boldsymbol{q_0} \\ \alpha_0 \end{pmatrix}^{n} - \eta^{n+1} \begin{pmatrix} \frac{\partial \mathcal{R}}{\partial \boldsymbol{q}} & \frac{\partial \mathcal{R}}{\partial \alpha} \\ \frac{\partial C_L}{\partial \boldsymbol{q}} & \frac{\partial C_L}{\partial \alpha} \end{pmatrix}^{-1} \begin{pmatrix} \mathcal{R}(\boldsymbol{q_0}^n, \alpha_0^n) \\ C_L(\boldsymbol{q_0}^n, \alpha_0^n) - C_L^t \end{pmatrix}. \tag{10}$$

### 2.3 Global stability analysis

Following the governing equations 7, in a linear framework we can decompose the state vector $\boldsymbol{q}$ as

$$\boldsymbol{q}(x, y, z, t) = \boldsymbol{q_0}(x, y, 0) + \epsilon\, \boldsymbol{q'}(x, y, z, t), \quad \boldsymbol{q'}(x, y, z, t) = \hat{\boldsymbol{q}}(x, y) e^{\lambda t} e^{i\beta z} + c.c. \tag{11}$$

where $\epsilon \ll 1$, $\boldsymbol{q'}(x, y, z, t)$ is the linear perturbation and $\boldsymbol{q_0}(x, y, 0)$ is the two-dimensional steady state solution of the governing equations ($\mathcal{R}(\boldsymbol{q_0}, \alpha_0) = \boldsymbol{0}$). Here the three dimensional perturbation fields $\boldsymbol{q'}$ have been decomposed in a normal form, where $\hat{\boldsymbol{q}}(x, y)$ is a complex mode associated to the eigenvalue $\lambda = \sigma + i\omega$ and the transverse wavenumber $\beta$ in the $z$ direction. The temporal evolution of three-dimensional perturbations characterized by the wavelength $\lambda_z = 2\pi/\beta$ is then given by the growth rate $\sigma$ and frequency $\omega$. By injecting the decomposition into the governing equations 7 we arrive to the following generalized eigenvalue problem

$$\lambda \mathcal{M} \hat{\boldsymbol{q}} = \mathcal{L}^\beta \hat{\boldsymbol{q}} \tag{12}$$

where $\mathcal{L}^\beta = \frac{\partial \mathcal{R}}{\partial \boldsymbol{q}}(\boldsymbol{q_0}, \alpha_0, \beta)$ is the Jacobian operator around the steady-state $\boldsymbol{q_0}$ which is a function of the transverse wavenumber $\beta$. The solution $\boldsymbol{q_0}$ is globally unstable in the asymptotic time limit if (at least) one eigenvalue $\lambda$ of $\mathcal{L}^\beta$ has a positive growth rate ($\sigma > 0$).

### 2.4 Numerical methods

The governing equations are discretized using continuous finite elements on an unstructured mesh. A typical mesh consists of approximately 350000 triangular elements and may be highly anisotropic near the airfoil. The anisotropy of the mesh is controlled and adapted to the Hessian of the velocity and eddy-viscosity fields but also to sensitivity fields related to the global modes, in order to ensure converged stability results. Due to the convection-dominated flow, the classical Galerkin formulation here is stabilized using the Streamline Upwind Petrov–Galerkin method [9]. The assembly, factorization and the inversion of all linear operators for the linear and nonlinear problems is fully parallel using the PETSc interface in FreeFEM. To determine the leading eigenvalues in eigenvalue problems, we rely on a shift-and invert strategy and the Krylov–Schur subspace method using the SLEPc interface implemented in FreeFEM.

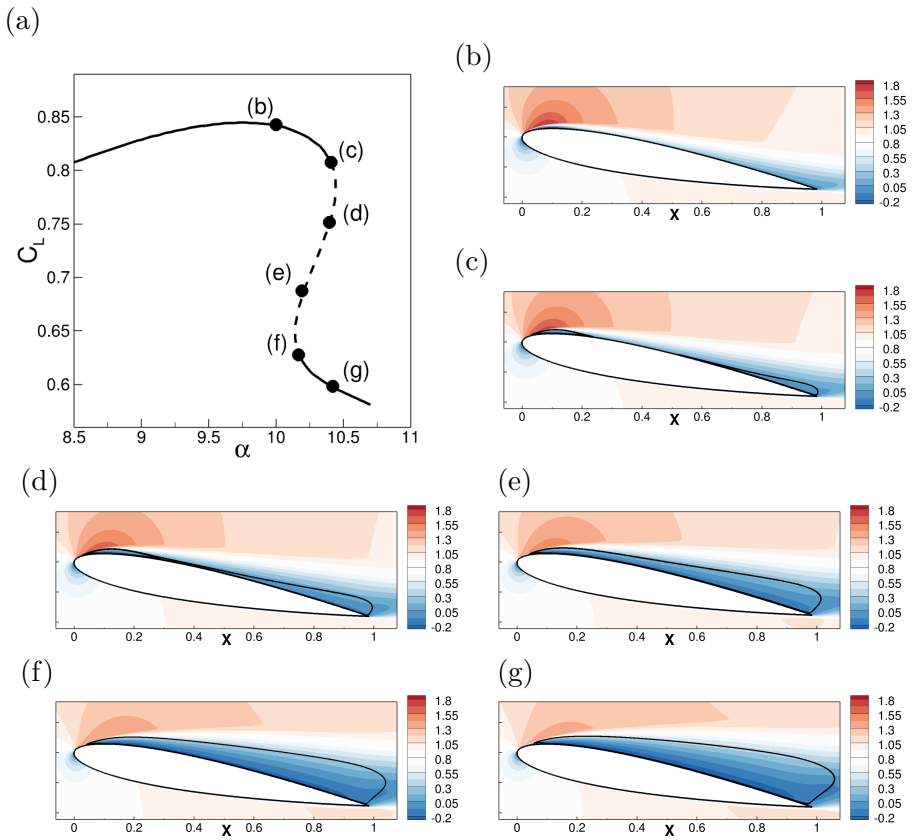


**Figure 1**: Steady-state solutions of the transitional flow around the airfoil at Reynolds number $Re = 90000$ near stalling angles of attack. (a) Evolution of the lift coefficient $C_L$ as a function of the angle of attack $\alpha$ in the high angle of attack range $8.5° \leq \alpha \leq 11°$ . The branch of globally unstable solutions are shown using a dashed line. (b-g) Streamwise velocity components $\bar{u}$ corresponding to their associated steady-state solutions marked with filled circles on (a). A black line shows the dividing streamline of the separated flow.

## 3 RESULTS

### 3.1 Steady solutions around stall and static hysteresis

Steady-state solutions of the transitional flow configuration have been obtained by fixed point solutions of eq. 7 for different angles of attack. In this paper we will focus on solutions at high angles of attack, corresponding to stalling regimes. As mentioned in §2.2, a continuation method is employed to allow us to move along the space of $C_L$ and obtain branches of co-existing solutions for the same angle of attack $\alpha$. Figure 1(a) shows the evolution of the lift coefficient $C_L$ as a function of the angle of attack $\alpha$, in the range $8° \leq \alpha \leq 11°$. In the pre-stalling regime ($\alpha \leq 10°$), the lift coefficient grows linearly with respect to the angle of attack. Moving close to the stall regime though ($\alpha \geq 10°$) we observe a sudden drop of the lift coefficient, where co-existing steady-state solutions for the same angle of attack exist, forming a characteristic S-shaped curve. Three branches of steady solutions can be identified, a high-$C_L$ branch ($9° \leq \alpha \leq 10.25°$) before stall, a low-lift branch ($\alpha \geq 10.25°$) after stall and a mid-$C_L$ branch connecting the two. As it will be discussed on §3.2, solutions on the mid-$C_L$ branch

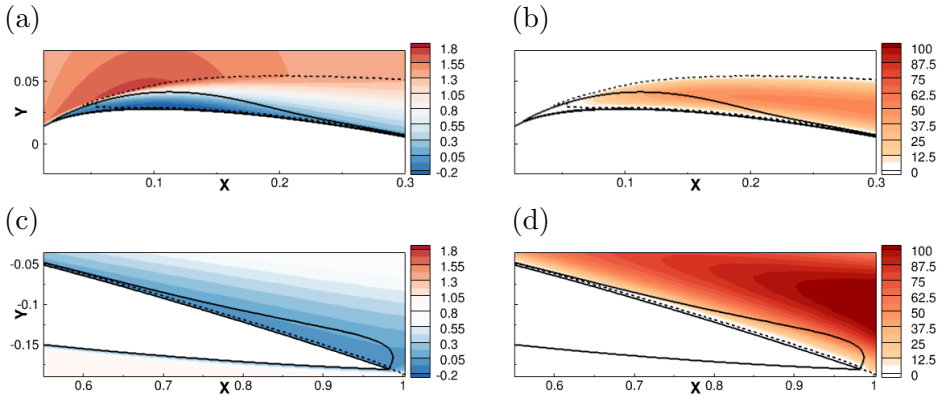


**Figure 2**: Steady-state high-$C_L$ solution at $Re = 90000$ for $\alpha = 10.4°$ and $C_L = 0.805$, corresponding to the solution of figure 1(c). (a,c) Streamwise velocity $\bar{u}$ and (b,d) mean eddy-viscosity $Re \cdot \bar{\nu}_t$ normalized by the kinematic viscosity $\nu = 1/Re$. A solid line corresponds to the dividing streamline of the separated flow, delimiting the LSB at the leading edge and the TSB at the trailing edge. A dashed line corresponds to the isoline $\gamma = 1$ of the intermittency function $\gamma$, marking the transition to turbulence.

are globally unstable to two-dimensional perturbations and are therefore plotted using dashed lines on figure 1. Such co-existing solutions around stall were first identified on a turbulent NACA0012 airfoil by [10] and later by [3] on a OA209 airfoil exhibiting trailing edge stall and are related to the static hysteresis phenomenon. In this work, the convergence of the mid-$C_L$ branch was possible due to the use of the continuation method in §2.2, since a marching on the angle of attack $\alpha$ would drop us from the high-$C_L$ branch directly to the low-$C_L$ branch. The topology of the associated steady solutions is shown on figures 1(b-g), displaying the streamwise velocity $\bar{u}$ for the corresponding angles of attack marked with filled circles on figure 1(a). On these contour fields, solid black lines show the dividing streamline of the recirculating flow, delimiting attached from separated regions. At the pre-stall regime ($\alpha \lessapprox 10°$) at the angle $\alpha = 10°$ (figure 1(b)), the flow is mostly attached on the suction side of the airfoil. Moving closer to the stalling regime, flow separation starts to develop at the leading and trailing edge of the airfoil; Specifically, we focus in figure 2 on the steady solution for the angle of attack $\alpha = 10.4°$ that is corresponding to the solution of figure 1(c). We notice in 2(a) that the laminar boundary layer separates at the chord-wise position $x_c \sim 0.02$ near the leading edge and reattaches at $x_c \sim 0.25$ in a turbulent manner forming a laminar separation bubble (LSB), delimited by the dividing streamline of the separated shear layer. To further comment on the nature of separation and reattachment, on figure 2(b) we show contours of the eddy-viscosity field $\nu_t/\nu$ normalized by the kinematic viscosity $\nu$. A dashed line corresponds to the isoline of $\gamma = 1$, marking the transition to turbulence where production of $\nu_t$ is activated. We see that production does not start before $x_c \sim 0.04$ and that the levels of $\nu_t/\nu$ are negligible near the leading edge, meaning that boundary layer that separates is laminar. In the separated shear layer, production of turbulence is activated and levels of $\nu_t/\nu$ rise, reattaching the boundary layer and forming an LSB. Similar to our analysis, a LSB is also captured on this airfoil configuration at the same Reynolds number by the LES simulations of [11]. Near the trailing edge (figures 2(c,d)), the turbulent boundary layer separates at $x_c \sim 0.65$ and reattaches at the edge of the airfoil, forming a turbulent separation bubble (TSB). Moving further along the branches of

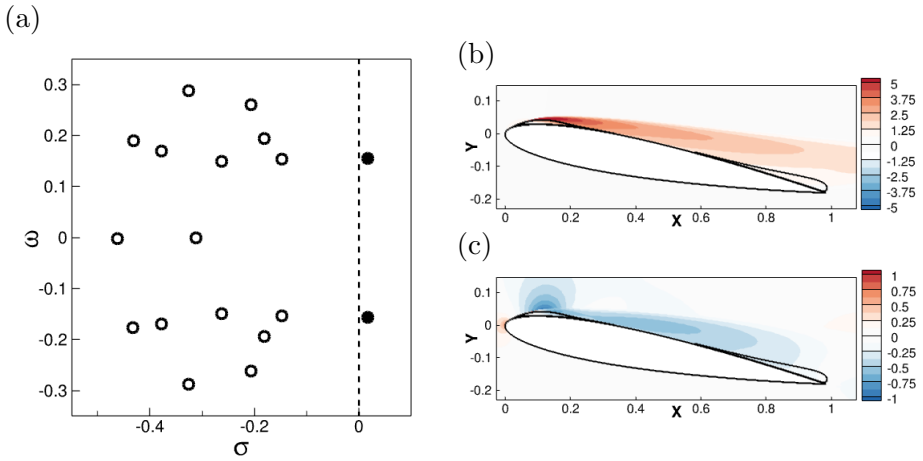


**Figure 3**: Stability analysis results of the high-$C_L$ solution at $\alpha = 10.4°$ and $C_L = 0.805$. (a) Eigenspectrum of leading eigenvalues around $\omega = 0$. Stable eigenvalues are depicted with open circles. The low-frequency ($\omega = 0.16$) unstable eigenvalues are depicted with filled blue circles. (b) real part of streamwise velocity $\Re(\hat{u})$ and of (c) cross-stream velocity $\Re(\hat{v})$ components of the unstable global mode. The mode has been normalized such that $< \hat{\boldsymbol{u}}, \hat{\boldsymbol{u}} >= 1$.

steady solutions on figures 1(c-e), the reattachment point of the LSB and the detachment point of the TSB move closer together until they merge, forming a large recirculation region on figure 1(d) and going towards a massively separated state on figure 1(g). This separation scenario is associated with a combined leading-edge trailing-edge stall mechanism ([12]).

### 3.2 Global stability to two-dimensional perturbations

After obtaining fixed point solutions in §3.1 of the airfoil at stalling angles of attack, we proceed by studying their stability to two-dimensional perturbations. We therefore follow the stability formulation introduced in §2.3 by setting the spanwise wavenumber to $\beta = 0$. Figure 3 shows the global stability results of the high-$C_L$ fixed point at $\alpha = 10.4°$ and $C_L = 0.805$, corresponding to the solution of figure 2. On figure 3(a) we show the spectrum in the $\sigma - \omega$ plane of the leading eigenvalues where stable eigenvalues ($\sigma < 0$) are depicted with open circles while unstable ones ($\sigma \geq 0$) with filled circles. We notice two complex conjugate eigenvalues of low-frequency ($\omega = 0.16$) to be marginally unstable. The Strouhal number associated to this frequency based on the projected frontal area is $St = fcsin(\alpha)/U_0 \approx 0.021$. This loss of stability through the destabilization of a pair of complex conjugate eigenvalues is attributed to a Hopf bifurcation. The shape of the associated eigenfuction is shown on figures 3(b) and (c), showing the real part of streamwise $\Re(\hat{u})$ and (c) cross-stream $\Re(\hat{v})$ velocity of the unstable global mode $\hat{\boldsymbol{q}}$. Here the mode has been normalized to unit kinetic energy, i.e. such that $< \hat{\boldsymbol{u}}, \hat{\boldsymbol{u}} >= 1$, where $< a, b >= \int a^* \cdot b d\Omega$ corresponds to the Hermitian inner product. The structure of the mode is elongated along the streamwise direction and is clearly linked to the LSB at the leading edge, initiating at the laminar separation point and reaching its maximum value above the bubble. The cross-stream component is also located at the LSB and alternates in sign around the dividing streamline. This mode is similar to the stall mode found by [3] that in their study originated from the TSB at the trailing edge and is linked to the low-frequency oscillations phenomenon, driving the system towards a large-period limit cycle. In the comparable LES of [11] a low-

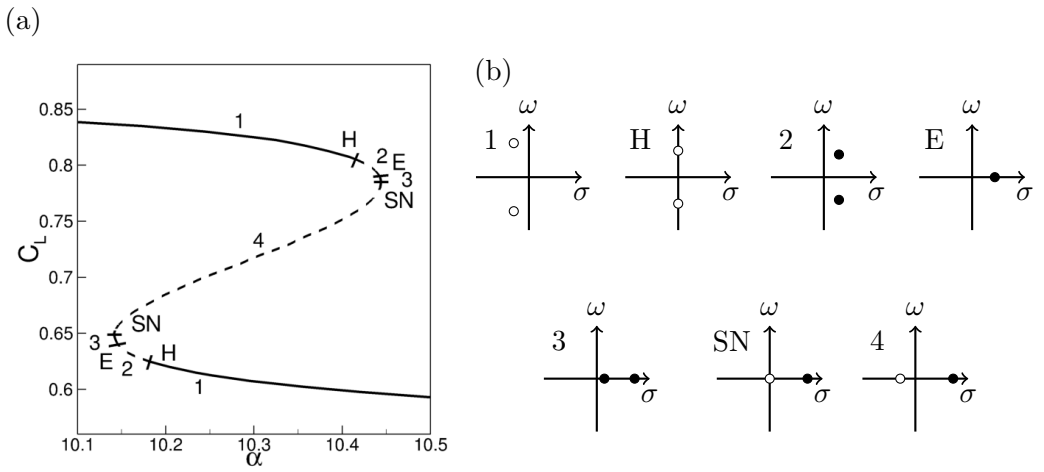


**Figure 4**: Bifurcations of the stall (low-frequency) eigenvalue along the steady flow solutions. (a) Lift $C_L$ versus the angle of attack $\alpha$ with the stable and unstable branches shown by solid and dashed curves, respectively. (b) Schematic representation of the low-frequency eigenvalue in the $\sigma$ versus $\omega$ plane showing the different stability regimes and bifurcations. Numbers indicate the different regimes while letters the bifurcation points (H for Hopf, SN for saddle-node and E for exceptional).

frequency oscillation of the flow is observed with a Strouhal number $St^{LES} = 0.024$, consistent with the present linear stability prediction ($St = 0.021$). We move now along the branches of steady solutions shown and track the path of the eigenvalues to identify critical bifurcation points. On figure 4(a) we show again the lift $C_L$ versus angle of attack $\alpha$ curve where letters denote the critical bifurcation points and numbers the different stability regimes. The position of the low-frequency eigenvalues is shown schematically on figures 4(b-h) for the different points. Starting from regime "1" where the flow is globally stable we move to the unstable regime "2" through a Hopf bifurcation (marked with "H") as described before. As we move further on the unstable branch, the complex conjugate eigenvalues increase in $\sigma$ but also move closer together (decrease in $\omega$) until they merge into a singular point; at this point the two eigenvalues and eigenvectors coalesce. This point is usually called an exceptional point (marked with "E"), common in non-Hermitian operators [13]. Following the exceptional point, the two eigenvalues separate again and one moves to the left (decreasing in $\sigma$) and one to the right (increasing in $\sigma$). This state of two unstable stationary ($\omega = 0$) eigenvalues is marked as "3" in the figure. As we further follow the branch, the left eigenvalue reaches and crosses the imaginary axis, becoming stable ($\sigma < 0$). At the critical point where $\lambda = 0$ (figure 4(g)) we have a saddle-node bifurcation (marked "SN"), characterized by two fixed points colliding and annihilating each other. The saddle-node point coincides exactly with the turning point ($\partial C_L/\partial\alpha = 0$) of the $C_L(\alpha)$ function. Note that converging the saddle-node point is non-trivial since the Jacobian matrix is not invertible ($\mathcal{L}$ has a zero eigenvalue) and convergence here was achieved by inverting the augmented Jacobian (equation 10). After the "SN" bifurcation, we move to the stability regime "4" where one eigenvalue is stable and one unstable. The same exact bifurcation paths occur in reverse order at the lower branch of the curve; a saddle-node bifurcation at the turning point, followed by an exceptional point and then a Hopf bifurcation back to a fully stable system. Interestingly, the same bifurcation scenario was obtained by [3] on a fully-turbulent airfoil flow exhibiting trailing-edge stall. This shows that the low-frequency phenomena in stalling airfoils

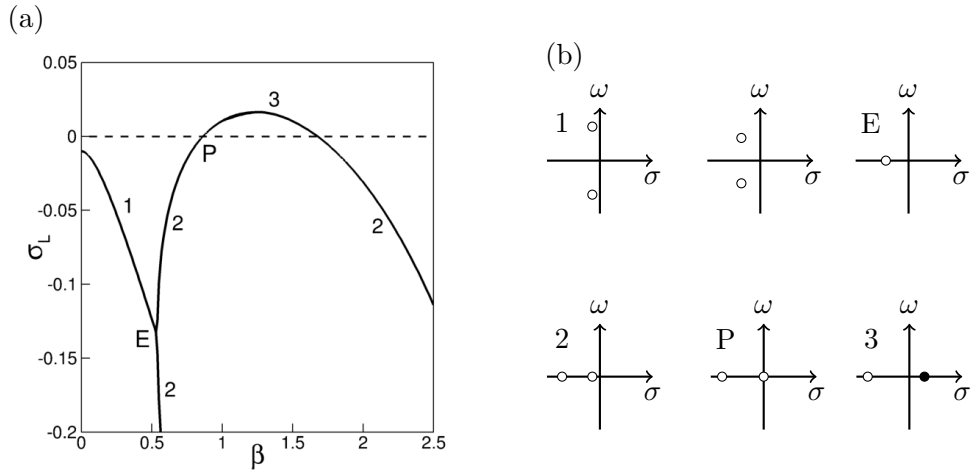


**Figure 5**: Continuation of the low-frequency eigenvalue to three-dimensions for the high-$C_L$ solution at $\alpha = 10.25°$ and $C_L = 0.81$. (a) Evolution of the growth rate $\sigma_L$ of the most unstable eigenvalues as a function of the transverse wavenumber $\beta$. (b-g) Schematic representation of the leading eigenvalues in the complex plain $\sigma$ versus $\omega$ showing the different stability regimes (numbers) and critical bifurcation points (E for exceptional and P for pitchfork) that are indicated on (a).

seem to be independent of the flow conditions (turbulent/transitional) or type of stall mechanism (leading-edge, trailing-edge or combined leading/trailing edge).

### 3.3 Global stability to three-dimensional perturbations

We now extend the analysis to three-dimensional perturbations by following again the stability formulation introduced in §2.3 but for non-zero spanwise wavenumbers $\beta$. We start our analysis here with the high-$C_L$ solution at $\alpha = 10.25°$ and $C_L = 0.81$. This state is just before the Hopf bifurcation (which occurs for $C_L = 0.805$) and corresponds to the stability regime marked "1" in figure 4 where the flow is globally stable and the leading eigenvalues are close to criticality. We depart from the two-dimensions ($\beta = 0$) be increasing the wavenumber $\beta$ in the range $0 \leq \beta \leq 2.5$ and track the complex eigenmodes. Figure 5(a) shows the growth rate $\sigma_L$ of the aforementioned leading eigenvalue as a function of $\beta$. Numbers indicate again the different stability regimes while letters the critical points. Figures 5(b-g) represent schematically the position of the leading eigenvalues in the complex plain for the different regimes. Starting from the globally stable region "1", increasing $\beta$ results in the conjugate eigenvalues decreasing in $\sigma$ and $\omega$, moving closer together until they coalesce to a singular point for $\beta = 0.5$. This point is an exceptional point, marked with "E", similar to the one found in §3.2. By further increasing $\beta$, the steady now ($\omega = 0$) eigenvalues repel each other, one decreasing and one increasing in $\sigma$ until for $\beta = 0.75$ now reaches and crosses the imaginary axis (figure 5(f)), becoming globally unstable. This loss of stability is related to a pitchfork bifurcation, marked with "P" in the figure, which breaks the symmetry of the flow in the third dimension. We notice that by further increasing $\beta$ the growth rate of the unstable mode saturates at $\beta = 1.25$ and then decreases again, crossing the imaginary axis to a globally stable state. The wavenumber at maximum amplification corresponds to a very large transverse wavelength $\lambda_z = 2\pi/\beta \sim 5$, i.e. a wavelength of 5 times the chord $c$.

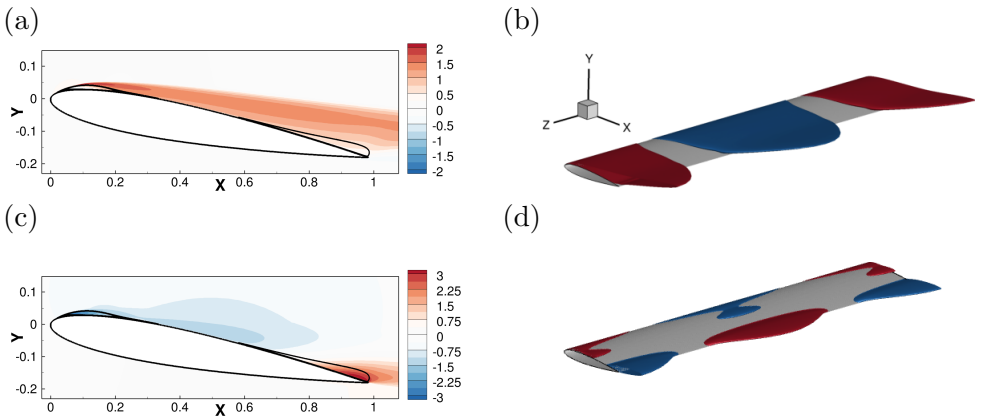


**Figure 6**: Spatial structure of the steady ($\omega = 0$) global mode for the wavenumber $\beta = 1.25$. (a,c) Planar and (b,d) three-dimensional views of the (a,b) streamwise velocity $u'$ and (c,d) spanwise velocity $w'$. Isosurfaces correspond to (b) $u' = \pm 1$ and (d) $w' = \pm 2$. The mode has been normalized such that $< \hat{\boldsymbol{u}}, \hat{\boldsymbol{u}} >= 1$. The spatial extent of the domain in the transverse direction is $L_z = \lambda_z$ where $\lambda_z = 2\pi/\beta$.

The associated structure of the three-dimensional mode $\hat{\boldsymbol{q}}$ is shown on figure 6 for the wavenumber of maximum amplification $\beta = 1.25$, using planar views (a,c) and isosurfaces (b,d) of the (a,b) streamwise velocity perturbation ($u' = \frac{1}{2}(\hat{u}e^{i\beta z} + c.c.) = \pm 1$) and (c,d) transverse velocity perturbation ($w' = \frac{1}{2}(\hat{w}e^{i\beta z} + c.c.) = \pm 2$). The mode has been normalized such that $< \hat{\boldsymbol{u}}, \hat{\boldsymbol{u}} >= 1$ while the wing here has an extent of $L_z = \lambda_z = 2\pi/\beta$ in the spanwise direction. The shape reveals elongated structures of streamwise velocity $\hat{u}$ that originate at the LSB and decay as we move downstream. The transverse component $\hat{w}$ is very strong and connects the LSB at the leading edge and the TSB at the trailing edge, alternating in sign between the two. This mode bears similarities with the three-dimensional mode found by [6] on a fully turbulent NACA4412 airfoil at $Re = 350000$ that is linked to the formation of stall cells, which periodically modulate the separated flow in the spanwise direction. The wavelength here though $\lambda_z \sim 5$ is much higher than the wavelengths of stall cells commonly found in literature ($\lambda_z \sim 1$), not excluding the possibility of this being linked to a phenomenon that is rarely observed due to its extremely large wavelength. Furthermore, since the three-dimensional mode is a continuation of the low-frequency mode for $\beta \neq 0$ it suggests that these two instabilities might be linked.

We have therefore identified that this steady solution, which is globally stable to two-dimensional perturbations, gets unstable to a three-dimensional mode; thus the three-dimensional instability precedes the two-dimensional one. It is of interest to further analyze this and identify how these modes compete along the hysteresis curve. On figure 7(a) we show again the lift-coefficient $C_L$ versus the angle of attack $\alpha$ where globally stable and unstable solutions are shown with solid and dashed lines respectively. The bifurcation path of the unsteady mode is shown on figure 7(b), reporting the growth rate $\sigma$ of the eigenvalues for the different values of $C_L$. Here, only the critical Hopf points are highlighted with "H". For the steady mode, since the $\beta$ of maximum amplification is $\beta = 1.25$ we expect that the critical pitchfork bifurcation occurs for that value. We therefore follow on figure 7(c) the growth rate $\sigma$ of the three-dimensional stationary mode at $\beta = 1.25$ along the branches of solutions. The bifurcation path of the unsteady mode is also shown in gray for comparison. The steady mode destabilizes first and is more amplified than the unsteady one, increasing its growth rate until it reaches a maximal value

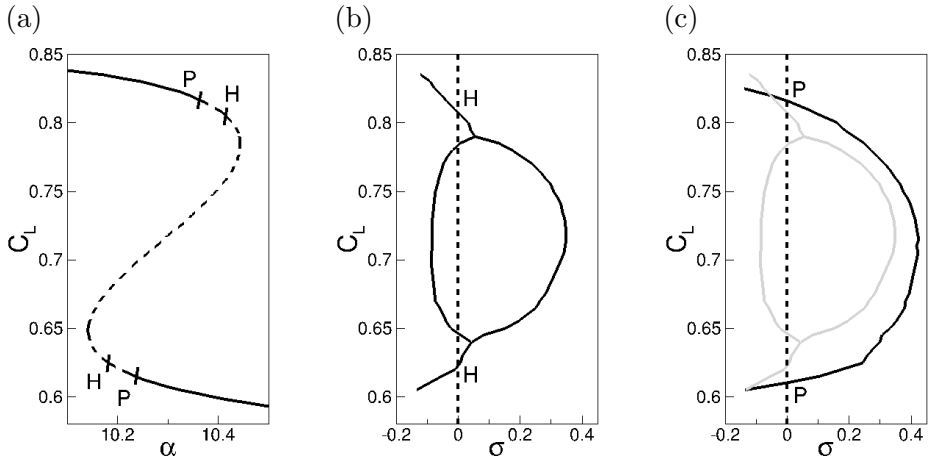


**Figure 7**: Competition between two-dimensional unsteady and three-dimensional steady modes. (a) Lift coefficient $C_L$ versus the angle of attack $\alpha$. Solid and dashed lines distinguish between globally stable and unstable solutions. (b) Growth rate $\sigma$ of the unsteady two-dimensional ($\beta = 0$) mode and (c) of the three-dimensional steady mode for $\beta = 1.25$ versus $C_L$. The critical bifurcation points (P for pitchfork and H for Hopf) are indicated on the figures. On (c) the path of the unsteady mode is also shown using a gray line for comparison.

at the center of the inverted-S curve. After that point, the growth rate decreases again until the mode stabilizes at the lower branch. In both the upper and lower branches, the pitchfork bifurcation precedes the Hopf, showing that the primary instability is the three-dimensional.

## 4 CONCLUSIONS

In this paper we performed global stability analyses of transitional flows around a NACA0012 airfoil at $Re = 90000$ and several angles of attack near stalling conditions. We modelled the transitional flow using a RANS framework, coupled with a Spalart-Allmaras turbulence model and an algebraic transition model. A continuation method allowed us to obtain unstable solutions near the stalling angle that form a characteristic inverted-S shape in the $C_L - \alpha$ plane, related to the hysteresis phenomenon. Global stability of these solutions revealed the existence of a two-dimensional unsteady mode related to the low-frequency oscillations phenomenon and of a three-dimensional steady mode with a very large transverse wavelength. By following the different modes along the inverted-S curve we have identified that the three-dimensional mode becomes unstable prior to the two-dimensional one in the present case. The flow becoming primarily three-dimensional suggests that low-frequency unsteadiness could occur as a secondary instability of the saturated three-dimensional state. Stability analysis of these three-dimensional states is a natural step for further exploring this scenario.

## 5 ACKNOWLEDGEMENTS

This project has received funding from the European Union's Horizon 2020 research and innovation program under the Marie Skłodowska-Curie grant agreement No 955923.

## REFERENCES


[1] Schmitz, F.W. 1967 Aerodynamics of the model airplane. Part I. Airfoil measurements. *NASA Tech. Memo.* 60976.

[2] Zaman, K.B.M.Q., Bar-Sever, A. & Mangalam, S.M. 1987 Effect of acoustic excitation over airfoils near stall. *J. Fluid Mech.* 182, 127–148.

[3] Busquet, D., Marquet, O., Richez, F., Juniper, M. & Sipp D. 2021. "Bifurcation Scenario for a Two-Dimensional Static Airfoil Exhibiting Trailing Edge Stall." *J. Fluid Mech.* 928: A3.

[4] Gregory, N., Quincey, V.G., O'Reilly, C.L. & Hall, D.J. 1970 Progress report on observations of three-dimensional flow patterns obtained during stall development on aerofoils, and on the problem of measuring two-dimensional characteristics. Tech. Rep. CP 1146. Aeronautical Research Council.

[5] Moss, G.F. & Murdin, P.M. 1971 Two dimensional low-speed tunnel tests on the NACA 0012 section including measurements made during pitching oscillations at the stall. Tech. Rep. CP 1145. Aeronautical Research Council.

[6] Plante, F., Dandois, J., Beneddine, S., Laurendeau, É. & Sipp, D. 2021 Link between subsonic stall and transonic buffet on swept and unswept wings: from global stability analysis to nonlinear dynamics.*J. Fluid Mech.* 908, A16.

[7] Spalart, P.R. & Allmaras, S.R. 1994 A one-equation turbulence model for aerodynamic flows. *La Rech. Aérosp.* 1, 5–21.

[8] Cakmakcioglu, S. C., Bas, O., Mura, R., and Kaynak, U. 2020, A Revised One-Equation Transitional Model for External Aerodynamics. *AIAA Paper* 2020-2706.

[9] Tezduyar, Tayfun E 1991 Stabilized finite element formulations for incompressible flow computations. *Advances in applied mechanics* 28, 1–44.

[10] Wales, C., Gaitonde, A.L., Jones, D.P., Avitabile, D. & Champneys, A.R. 2012 Numerical continuation of high Reynolds number external flows. *Intl J. Numer. Meth. Fluids* 68, 135–159

[11] ElAwad YA, ElJack EM. Numerical investigation of the low-frequency flow oscillation over a NACA-0012 aerofoil at the inception of stall. *International Journal of Micro Air Vehicles.* 2019;11.

[12] McCullough, G.B. & Gault, D.E. 1951 Examples of three representative types of airfoil section stall at low speed. *NACA Tech. Note* 2502.

[13] Meng H., Ang, Y.S., Lee, C.H. 2024 Exceptional points in non-Hermitian systems: Applications and recent developments. *Appl. Phys. Lett.* 5 February 2024; 124 (6): 060502.